HYPERTHERMIA STUDIES OF FERRITE NANOPARTICLES SYNTHESIZED IN THE PRESENCE OF COTTON

Journal:	*New Journal of Chemistry*
Manuscript ID:	NJ-ART-01-2015-000009.R2
Article Type:	Paper
Date Submitted by the Author:	01-Jul-2015
Complete List of Authors:	Carvalho, Maria Deus; CQB- FCUL, Mendo, Sofia; CQB-FCUL, Alves, Andre; CQB-FCUL, Ferreira, Liliana; BioISI-FCUL, Cruz, Maria; BioISI-FCUL, Mendonça, Maria; CQB-FCUL, Godinho, Margarida; BioISI-FCUL,

HYPERTHERMIA STUDIES OF FERRITE NANOPARTICLES SYNTHESIZED IN THE PRESENCE OF COTTON

Sofia G. Mendo,[a] André F. Alves,[a] Liliana P. Ferreira,[b,c] Maria Margarida Cruz,[b] Maria Helena Mendonça,[a] Margarida Godinho,[b] and Maria Deus Carvalho[a*]

[a]*Centro de Química e Bioquímica (CQB), Faculdade de Ciências, Universidade de Lisboa, Campo Grande, 1749-016 Lisboa, Portugal.*

[b]*Biosystems and Integrative Sciences Institute (BioISI), Faculdade de Ciências, Universidade de Lisboa, Campo Grande, 1749-016 Lisboa, Portugal*

[c]*Department of Physics, University of Coimbra, 3004-516 Coimbra, Portugal*

Keywords: magnetic hyperthermia; cotton template; ferrite nanoparticles

Corresponding Author

*** Dr. Maria Deus Carvalho**
Address: DQB- FCUL, Campo Grande, C8, 1749-016 Lisboa
Contacts:
Phone: (+351) 217500954
Fax: (+351) 217500088
Email: mdcarvalho@ciencias.ulisboa.pt

Abstract

MFe_2O_4 (M = Co, Fe, Mn) compounds were synthesized using a hydrothermal treatment in the presence of medicinal cotton. Two sets of nanoparticles were produced for each composition and subsequently characterized by XRD, TEM and SEM. The nanoparticles obtained from the solution display the expected spinel structure and different mean sizes (below 16 nm); the nanoparticles embedded in cotton were submitted to a calcination process for cotton elimination. Regarding these calcinated samples, the spinel structure was maintained for $CoFe_2O_4$, a mixture of phases was identified for M = Mn sample and, in the case of iron, the magnetite phase was converted to hematite (α-Fe_2O_3). After cotton elimination the samples exhibit a morphology which evidences the role of cotton as template. To evaluate the quality of the nanoparticles for hyperthermia, SQUID magnetometry and Mössbauer spectroscopy were used to perform the magnetic characterization of all products and specific loss power (SLP) was determined by induction heating measurements. All the ferrite NP obtained by hydrothermal synthesis in the presence of cotton display good hyperthermia performance. $MnFe_2O_4$ nanoparticles exhibit the highest SLP value, 90 W g^{-1}, followed by $Fe_{3-x}O_4$, and $CoFe_2O_4$. In the case of $CoFe_2O_4$, the specific loss power of the NP obtained after cotton elimination is enhanced by 50% which is explained by the NP morphology adopted from the cotton template during the synthesis.

1. Introduction

Metal oxide nanoparticles with the spinel structure, AB_2O_4, have been largely investigated due to their potential for magnetic storage applications and, more recently, as excellent candidates for contrast enhancement in magnetic resonance imaging (MRI), drug delivery, and other biomedical uses. Taking advantage of their magnetic features, magnetic ferrites have also been explored as catalysts in processes such as methanol decomposition or hydroformylation reactions [1,2], as well as chemosensors and adsorbents in environmental and biological fields. [3] The biocompatibility of iron oxide nanoparticles associated with the attractive magnetic properties of some ferrites, have led to the discovery of new applications of nanoparticles in the medical field. [4-10] One of these applications is magnetic hyperthermia for cancer therapy, using the magnetic nanoparticles in an external oscillating magnetic field as local heat dissipating agents. [11]

Spinel ferrite nanoparticles have been synthesized by several methods such as co-precipitation, hydrothermal synthesis, thermal decomposition of suitable precursors, combustion reaction, sol-gel methods, reverse micelles technique, among others [12-17], the most common methods being the co-precipitation and thermal decomposition. Usually thermal decomposition provides a better way for tailoring the characteristics of the nanoparticles (NP), including the morphology, dimension and size dispersion. However, the costs associated and the use of hazardous reagents and solvents are negative points of this kind of synthesis. On the other hand, the co-precipitation method is one of the simplest, cheapest and most eco-friendly procedures. [16,17] Although the control of particle size and crystallinity is not well established, hydrothermal treatments can improve the magnetic properties of the NP due to the synergistic effect of temperature and pressure. [17]

The use of hydrothermal treatments to obtain magnetite, maghemite or other ferrites has been largely explored and it has been shown that the temperature, treatment time and pH values influence the size of the obtained nanoparticles [13,18-21]. For instance, magnetite nanoparticles with a mean size of 39 nm were obtained using a hydrothermal treatment at 250 ºC for 24 h [13] while performing a treatment of 2h at 200ºC resulted in maghemite nanoparticles with sizes between 10 and 110 nm, depending on the incubation time (at 200ºC) an the pH of the solution. [18] In the case of the cobalt ferrite, nanoparticles with mean sizes from 10 nm to 13 nm were obtained depending on the thermal treatment (100 ºC; 2 h and 200 ºC; 120 h respectively) [20] while $MnFe_2O_4$ nanorods with an average diameter of 20 nm and 250 nm of length were synthesized by a hydrothermal process at 180 °C after 12 h. [22]

In an attempt to explore new synthesis methods to control the nanoparticles size and morphology in the search for suitable materials for magnetic hyperthermia, cotton was used as a template to prepare MFe_2O_4 (M = Fe, Co, Mn) ferrites. This easy and inexpensive method, previously reported for the synthesis of NiO, MnO_2 and $NiFe_2O_4$ [23-25] allowed to obtain nanoparticles with enhanced properties (such as antibacterial activity, magnetism and photocatalytical performance), when compared to the material synthesized without the cotton template. These results were attributed to the samples microstructure induced by this methodology.

The structure and morphology of the synthesized MFe_2O_4 (M = Fe, Co, Mn) ferrites were investigated by powder X-ray diffraction and by scanning and transmission electron microscopy (SEM and TEM), and their magnetic properties by SQUID magnetometry and ^{57}Fe Mössbauer spectroscopy. Besides, the heating efficiency of the samples under the influence of an alternating magnetic field was evaluated in order to investigate their potential for magnetic hyperthermia.

2. Experimental

2.1 Synthesis of MFe_2O_4 nanoparticles (M = Fe, Co and Mn)

All compounds were synthesized by a standard precipitation method followed by a hydrothermal treatment during 3h at 150ºC, adopting a procedure already reported [14], this time in the presence of medicinal cotton.

In the case of magnetite, stoichiometric amounts of iron chloride ($FeCl_3.6H_2O$, Sigma-Aldrich), and iron sulphate ($FeSO_4.7H_2O$, Merck) were dissolved in distilled water under a nitrogen atmosphere and magnetic stirring. In the case of M = Co and Mn, iron nitrate ($Fe(NO_3)_3.9H_2O$) and cobalt nitrate ($Co(NO_3)_3.6H_2O$ from Sigma-Aldrich), and manganese chloride ($MnCl_2.4H_2O$) from Riedel-de-Haën, were used in stoichiometric amounts. In each synthesis, after complete dissolution of the two salts, ammonia solution (25%, Scharlau) was added to induce the formation of a precipitate. This mixture (precipitate and the remaining solution) was then transferred to an autoclave where medical cotton (around 3.5 g) was immersed, the complete procedure sequence being illustrated in figure 1. The autoclave was placed in an oven at 150 ºC for 3 hours. After cooling down to room temperature, the wet dark cotton was separated from the solution that clearly showed the presence of a magnetic black powder. This powder was separated using a commercial magnet, washed with distilled water until a neutral pH was obtained and dried at 60 ºC. As for the cotton embedded nanoparticles product, it was also washed and subsequently calcinated at 550 ºC for 6 hours in air, in order to eliminate the cotton. The temperature value of 550ºC was chosen after several tests with pure cotton in air, and corresponds to an almost complete elimination of cotton (less than 1% residues). Attempts to eliminate the cotton by thermal decomposition in

inert atmosphere were unsuccessful. Thus, each synthesis gave rise to two products, as summarized in table 1.

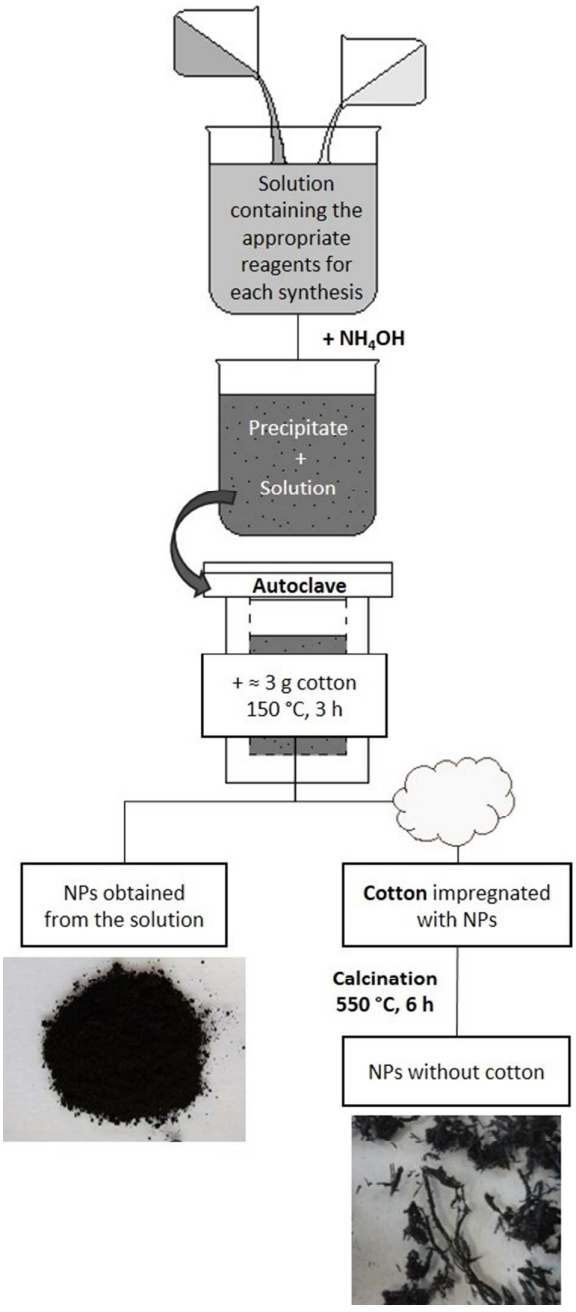

Figure 1- Schematic procedure of the MFe_2O_4 (M = Fe, Co, Mn) nanoparticles synthesis.

Table 1. Products obtained from the synthesis of MFe_2O_4 (M = Fe, Co, Mn) in the presence of cotton, following the procedure explained in the text and in figure 1. $<D_{XRD}>$ is the nanoparticles average diameter calculated from the XRD data using the Scherrer equation.

M	**Sample obtained**	**Product identified by XRD**	**$<D_{XRD}>$** / nm
Fe	from the solution	$Fe_{3-x}O_4$	13
	after cotton elimination	α-Fe_2O_3	43
Co	from the solution	$CoFe_2O_4$	7
	after cotton elimination	$CoFe_2O_4$	24
Mn	from the solution	$MnFe_2O_4$	16
	after cotton elimination	Mixture of phases	--

2.2 Structural and magnetic characterization

The structural characterization of all products was carried out by X-ray diffraction (XRD) using a Philips Analytical PW 3050/60 X'Pert PRO diffractometer equipped with a X'Celerator detector and with automatic data acquisition (X'Pert Data Collector software). A monochromatized CuKα radiation was used as incident beam. The diffractograms were obtained by continuous scanning in a 2θ - range from 10 to 80 º, with a scan step time of 40 s. The cell parameters were obtained by Rietveld refinement using the Fullprof software. [26] The average crystallite sizes were calculated from the broadening of the X-ray diffraction peaks using the Scherrer formula, $D = 0.89\ \lambda\ /\ \beta\ \cos\ \theta$, where λ is the wavelength of CuKα radiation and β is the full width at half maximum of the peak after line broadening correction.

The morphology of the samples was accessed by Scanning Electron Microscopy (SEM) and Transmission Electron Microscopy (TEM) using a JEOL 7001F and a Hitachi 8100 with digital image acquisition microscopes, respectively. The particles size distribution of the samples was determined statistically from the TEM images with the program ImageJ, by measuring the size of around 100 nanoparticles for each sample.

Magnetic characterization of all samples was performed using a SQUID magnetometer (QD-MPMS) and ^{57}Fe Mössbauer spectroscopy. Magnetization measurements were carried out as a function of temperature between 10 K and 400 K, at 5.0 mT, after cooling from room temperature in zero magnetic field (zero field cooled - ZFC) and after cooling under the measurement field (field cooled - FC). Hysteresis curves were obtained at different temperatures for applied magnetic fields up to 5.5 T. The ^{57}Fe Mössbauer spectra were collected at room temperature in transmission mode using a conventional constant-acceleration spectrometer and a 50 mCi ^{57}Co source in a Rh matrix. The velocity scale was

calibrated using an α-Fe foil. The spectra were fitted to Lorentzian lines, with distributions of the magnetic hyperfine field when justified, using the WinNormos Program.

2.3. Heating efficiency

Induction heating of the nanoparticles was performed using an Easy Heat 0224 device (Ambrell), under an AC field of 9.8 kA m^{-1} amplitude and 276 kHz frequency. Each compound was dispersed in 3 ml of a 5 % solution of sodium citrate in a glass container in a concentration of 1 mg/ml, sealed and immersed in an ultrasonic bath for 60 min. The bath temperature was kept constant by a continuous isothermal water flow. Immediately after, the samples were submitted to the magnetic oscillating field for 5 minutes while registering the dispersion temperature with an optical fiber probe (0.1 °C accuracy).

Special care was taken in evaluating the energy exchanges between the system (sample + container) and the environment, particularly to isolate the system from external heat sources. It was verified that although permanently cooled with running water the induction coils temperature attains high values (above 50ºC) and therefore should not be in direct contact with the solid thermal isolation. Energy exchanges under induction heating are much reduced by suspending the sample inside the coil and keeping it apart from the cooled coil by a 4 mm thick air layer plus a 12 mm thick thermal insulator layer and a 7 mm thick air layer. A schematic view of the setup is displayed in figure 2. The ensemble is isolated from external air convection by an acrylic box, and the environment temperature is monitored with a thermocouple. Several materials were tested as thermal insulator layers (figure 2 – a)), trying to improve the adiabatic conditions of the measurements. Figure 3-A compares the temperature decreasing rate of distilled hot water, placed in our system (applied magnetic field off) inside an eppendorf, for different insulator materials: expanded polyethylene (EPE),

polyurethane (PU), expanded polystyrene (EPS) and three different grain sizes of Portuguese cork (C1<C2<C3) (courtesy of *Amorim Cork Composites*). EPS and C3 are the materials that display lower thermal conductivity. However, when the field is on (9.8 kA m^{-1} amplitude and 276 kHz frequency), the specific capacity together with the thermal conductivity of C3 cork makes it less sensitive to the heating by the hot coils than EPS (figure 3-B). Therefore, C3 cork (ref. 8002, Amorim Cork Composites) was chosen for the experimental set-up.

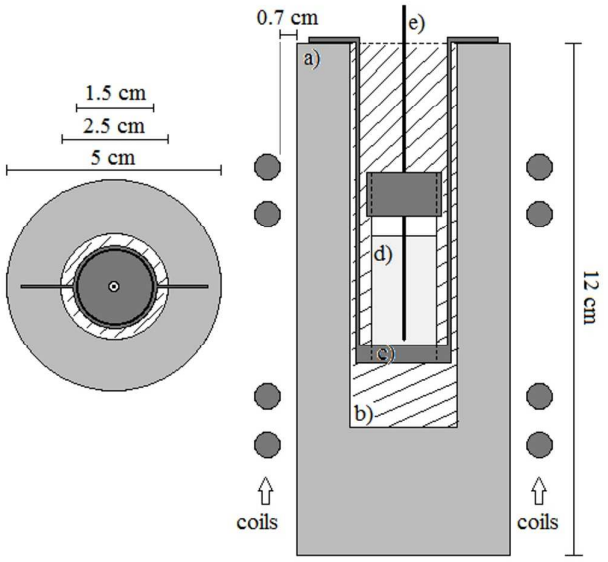

Figure 2 – Induction heating set-up: top (left) and axial (right) cross sections showing the position of the sample, sample holder and isolation layers inside the AC magnetic field coils; a) cork; b) air; c) nylon holder; d) sample in glass flask with lid; e) fiber optic temperature sensor.

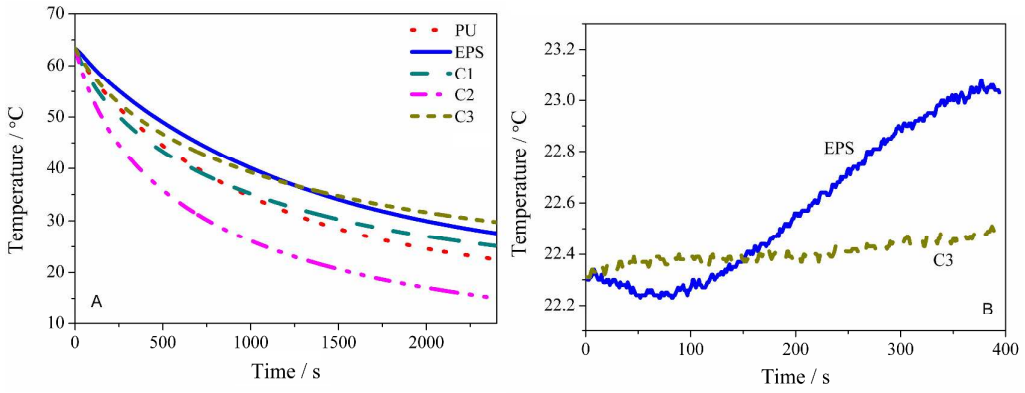

Figure 3- A) Evaluation of different materials for the thermal insulator a) in the set-up shown in figure 2, by comparing the energy losses of distilled water at 60ºC inside an eppendorf placed at the sample position (magnetic field off): expanded polyethylene (EPE), polyurethane (PU), expanded polystyrene (EPS) and three different grain size corks (C1<C2<C3) (Portuguese cork - courtesy of *Amorim Cork Composites*). B) Influence of the heat dissipated in the AC field coils (magnetic field on) on the temperature of distilled water initially at room temperature.

3. Results and Discussion

MFe_2O_4 (M = Co, Fe, Mn) nanoparticles were synthesized using a standard precipitation method followed by a hydrothermal treatment during 3h at 150ºC in the presence of medicinal cotton. As explained in section 2.1, this methodology gave rise to the production of two sets of nanoparticles for each preparation: those obtained from the solution and those embedded in cotton and further calcinated at 550 ºC for cotton elimination.

3.1 Structural and morphological characterization

Powder X-ray diffraction patterns of the products obtained from the solution revealed a unique crystalline phase for all samples (figure 4), as all peaks were attributed to the MFe_2O_4 spinel type structure (S.G. *Fd3m*). Mean particle sizes ($<D_{XRD}>$) of 13, 7 and 16 nm were estimated by the Scherrer equation, respectively for magnetite, Co and Mn ferrites (table 1). The mean sizes of magnetite and cobalt ferrite are smaller than those obtained using different hydrothermal treatments with higher temperatures [13,18,20].

The calculated cell parameters for MFe_2O_4, 8.375(1) Å, 8.370(1) Å and 8.477(1) Å for M = Fe, Co and Mn, respectively, are slightly smaller than those reported for the correspondent bulk ferrites, respectively, 8.396 Å, 8.391 Å and 8.499 Å (JCPDS files 19-629, 22-1086 and 10-0319). In the case of magnetite, the cell parameter depends on the nanoparticles' size and also on the Fe^{2+} content, the value determined for these samples being comparable to those obtained for samples with similar mean size and surface oxidation. In fact, these compounds have been better described as oxidized magnetite, $Fe_{3-x}O_4$. [13,14,27]

The smaller values of the cell parameters of $MnFe_2O_4$ and $CoFe_2O_4$ when compared with those reported in the JCPDS files can be explained by a different distribution of the metal ions among the tetrahedral and octahedral sites of the spinel structure. In the case of $CoFe_2O_4$, a cell parameter value a = 8.3777 Å, close to the one obtained in this work, was reported for 6 nm nanoparticles prepared by thermal decomposition, for which the distribution of the metal ions was determined by neutron diffraction as $(Fe_{0.73}Co_{0.27})[Fe_{0.63}Co_{0.37}]_2O_4$. [28]

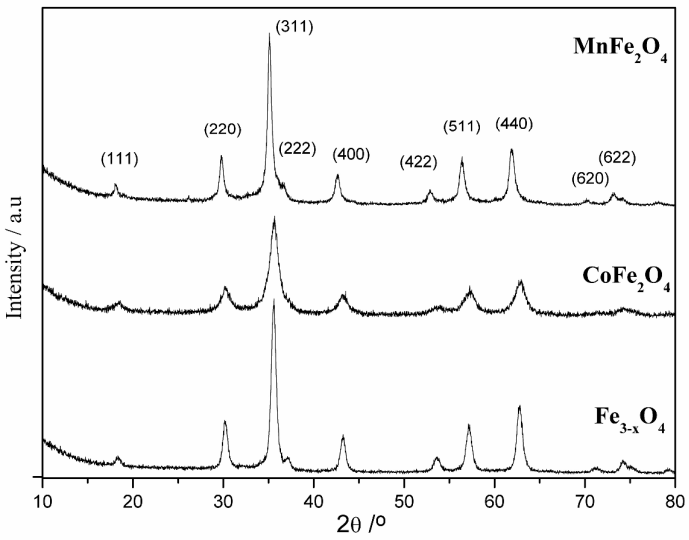

Figure 4. XRD patterns of the samples obtained from the solution.

From the wet black cotton, after cotton elimination by calcination in air at 550ºC, extremely fine powders were obtained in all cases. The powders were coloured black in the case of the cobalt and manganese compounds, and brick red in the case of the iron compound. The XRD analysis, figure 5, allowed to identify the cobalt and iron compounds as being single phased $CoFe_2O_4$ and hematite (α-Fe_2O_3, rhombohedral structure), respectively, in accordance with the JCPDS file nº 24-0072. The mean crystallite sizes for $CoFe_2O_4$ and α-Fe_2O_3 were determined to be 24 nm and 43 nm, respectively. In the case of the manganese compound, a mixture of Mn_2O_3, hematite and magnetite type phases was detected in the XRD diffractogram (not shown). As referred above, attempts to eliminate the cotton by thermal decomposition under inert atmosphere, avoiding further oxidation or phase separation of the materials, were unsuccessful.

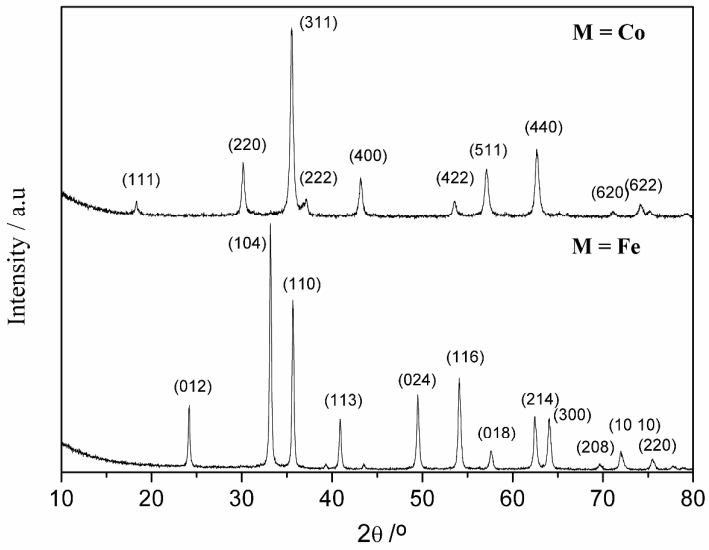

Figure 5. XRD patterns of the samples obtained after calcination of the wet cotton precursors: M = Co (up) and M = Fe (down), showing the characteristic peaks of a spinel ($CoFe_2O_4$) and hematite (α-Fe_2O_3) phases, respectively.

Figure 6 displays typical TEM images and the corresponding particle size distributions for MFe_2O_4 (M = Co, Fe, Mn) samples obtained from the solution, clearly showing the smaller size of the $CoFe_2O_4$ nanoparticles. While $Fe_{3-x}O_4$ and $CoFe_2O_4$ nanoparticles are relatively homogeneous, with mean sizes slightly smaller than those determined by XRD data, TEM images of $MnFe_2O_4$ reveal the presence of a bimodal distribution of nanoparticles centered in ~ 16 nm and ~ 5 nm. The value obtained by XRD data (16 nm) is in agreement with the larger NP mean size.

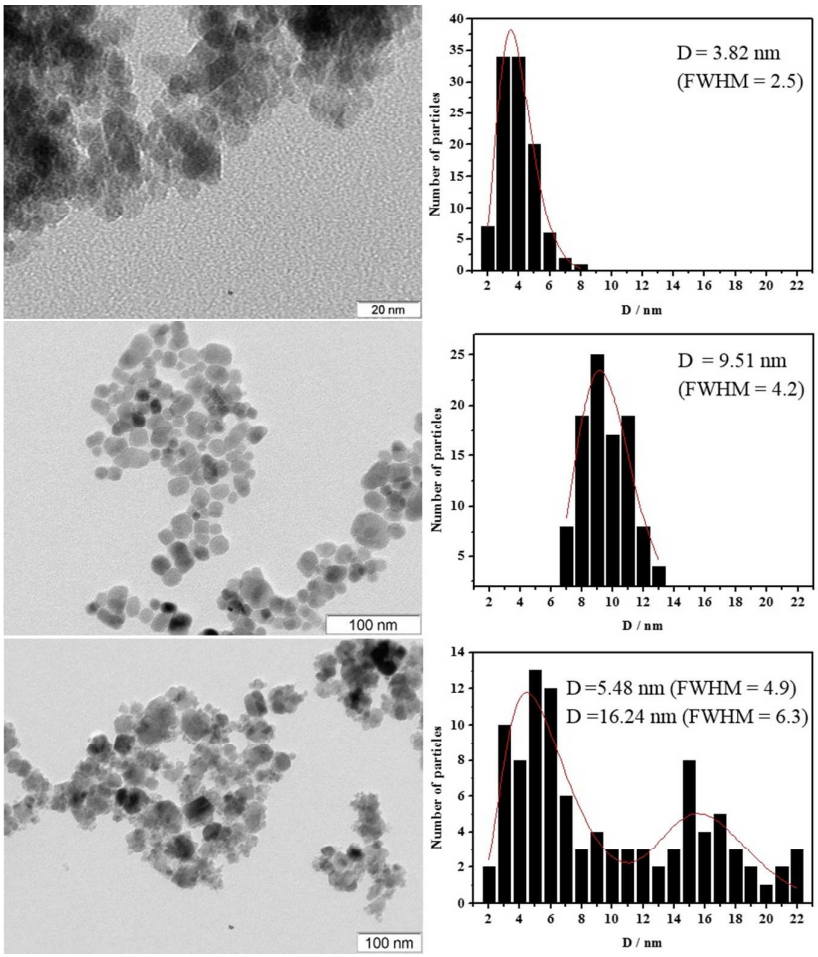

Figure 6. TEM images of the different nanoparticles obtained from the solution (left) and the corresponding size distribution histograms (right): $CoFe_2O_4$ (up); $Fe_{3-x}O_4$ (middle) and $MnFe_2O_4$ (down). The histograms were fitted with one ($CoFe_2O_4$and $Fe_{3-x}O_4$) or two ($MnFe_2O_4$) Log-Normal functions.

Representative SEM and TEM images of $CoFe_2O_4$ and α-Fe_2O_3 obtained after cotton elimination are shown in figure 7. The corresponding size distribution obtained for the $CoFe_2O_4$ sample is also displayed in figure 7.

The SEM image of $CoFe_2O_4$ clearly shows that the sample exhibit a peculiar morphology, indicating that the cotton shape was retained, as previously observed for NiO and MnO_2. [23,24]

Instead of individual nanoparticles, TEM images reveal that the samples consist of coalescent nanoparticles, with a mean size estimated to be around 8 nm for $CoFe_2O_4$. The significant difference when compared to that obtained by XRD (24 nm) clearly shows that the individual nanoparticles size is smaller than the crystallite size obtained by the Scherrer equation, indicating structural correlation between the different nanoparticles associated with the morphology of this sample. In the case of α-Fe_2O_3, TEM and SEM images show elongated coalesced particles making impossible the size distribution analysis, but clearly showing an average size larger than the one obtained for $CoFe_2O_4$.

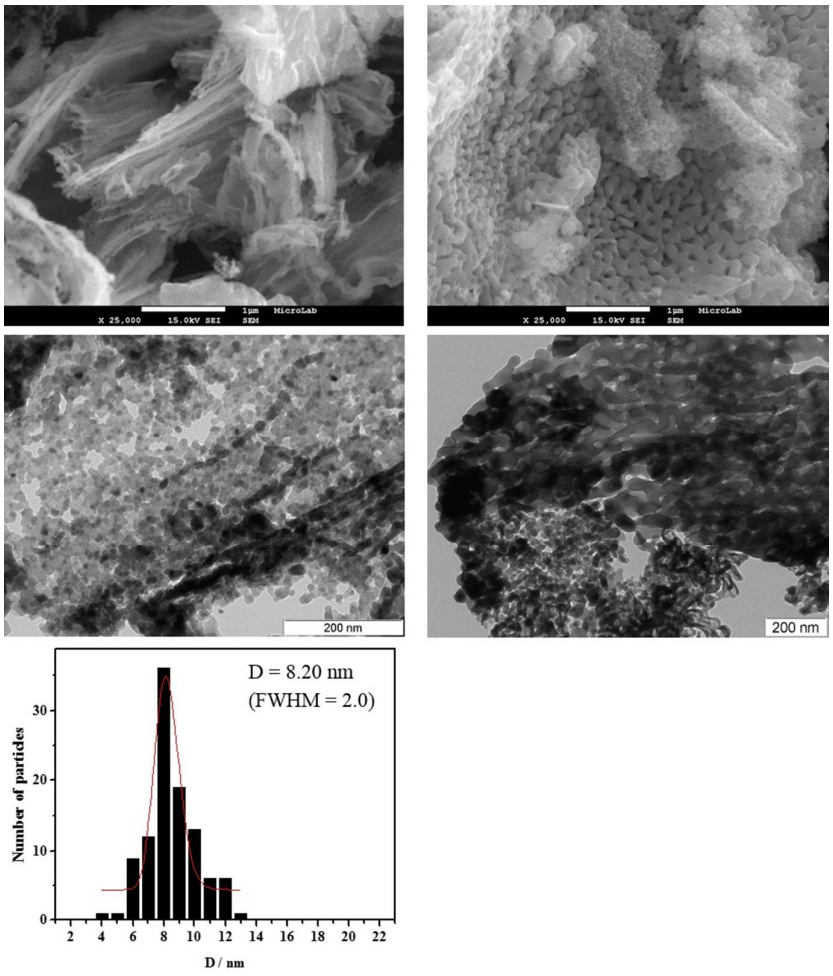

Figure 7. Results for $CoFe_2O_4$ (left) and α-Fe_2O_3 (right) samples obtained after cotton elimination: representative SEM (top) and TEM (middle) images and size distribution histogram for the cobalt ferrite (bottom). The histogram was fitted with one Log-Normal function.

3.2 Magnetic characterization

The MFe_2O_4 (M = Fe, Co, Mn) nanoparticles were characterized by SQUID magnetometry and ^{57}Fe Mössbauer spectroscopy.

As expected, the magnetization results of the NP obtained from the solution show that all samples are magnetic, the hysteresis curves being consistent with the ferrimagnetic behaviour of the bulk compounds. The magnetic parameters obtained from the experimental results (figure 8) are summarized in table 2.

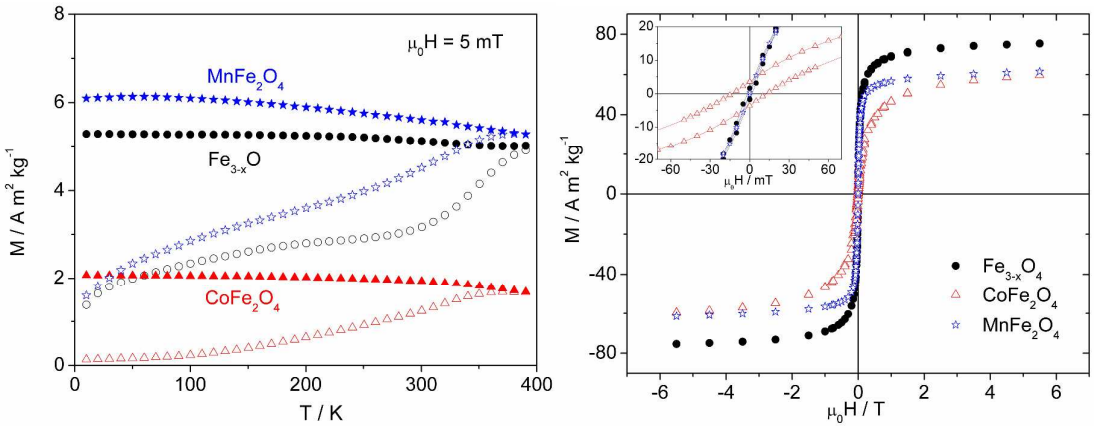

Figure 8. Temperature dependence of the magnetization (left) and hysteresis curves at 300 K (right) for the MFe_2O_4 (M = Co, Fe Mn) samples obtained from the solution.

The highest magnetization value (M_s) at 300 K obtained for $Fe_{3-x}O_4$ (75 A m^2 kg^{-1}), is around 80 % of the magnetite bulk value at room temperature (92 A m^2 kg^{-1} at 290 K [29]). Cobalt and manganese ferrites NP display lower magnetization values, 60 A m^2 kg^{-1} and 61 A m^2 kg^{-1} at 300 K, respectively, in agreement with the lower bulk magnetization values for these ferrites at 293 K (81 A m^2 kg^{-1} for $CoFe_2O_4$ [30] and 80 A m^2 kg^{-1} for $MnFe_2O_4$ [31]). The manganese ferrite magnetization values are higher than the values obtained for nanoparticles

with comparable mean sizes (16 nm) or larger. [32,33] In the case of the cobalt ferrite the values reported in literature are diverse [30,34-36] and similar magnetization values were reported for larger nanoparticles.

Only for the $CoFe_2O_4$ nanoparticles the ZFC curve presents a well-defined maximum in the temperature range of the measurements at 370 K. Only for the $CoFe_2O_4$ nanoparticles the ZFC curve presents a well-defined maximum in the temperature range of the measurements at 370 K. The maximum of the ZFC curve is often attributed to the blocking temperature and is very sensitive to dipolar interactions, being shifted to higher temperature with their increasing strength. Therefore the observed ZFC curves obtained from powder samples are consistent with NP exhibiting strong dipolar interactions. For both $MnFe_2O_4$ and $Fe_{3-x}O_4$ the ZFC magnetization increases gradually at low temperatures, displaying about 45% of the FC value at 100 K. For $CoFe_2O_4$ the ZFC magnetization is almost constant up to this temperature and attains the 45% FC relative value only at 250 K. This behavior along with the TEM results indicate a narrower distribution of magnetic moments in the case of the cobalt ferrite. The highest coercivity shown by the $CoFe_2O_4$ nanoparticles when compared to the other two samples can be associated to a higher magnetic anisotropy.

Table 2. Magnetic parameters at 300 K for samples MFe_2O_4 (M = Fe, Co and Mn) obtained from the solution. M_s: saturation magnetization; $\mu_0 H_c$: coercive field.

Sample	$\mathbf{M_s}$ /A m^2 kg^{-1}	$\mathbf{\mu_0 H_c}$ /mT
$\mathbf{Fe_{3-x}O_4}$	75	1
$\mathbf{CoFe_2O_4}$	60	13
$\mathbf{MnFe_2O_4}$	61	< 1

In general, in hyperthermia studies the AC magnetic field is far below the field needed to saturate the samples, although the heat dissipation depends on the maximum magnetization attained. It is therefore important to study the hysteresis loops in the range of magnetic field values used in hyperthermia to access the maximum value expected for the magnetization as well as to compare the DC energy losses. Although AC magnetic hysteresis areas are expected to be larger [37,38], the DC minor cycles give information for the relative losses of the three compounds. In this work an alternate sinusoidal magnetic field with amplitude of 9.8 kA m^{-1}, corresponding to 12.3 mT, was used. Hysteresis cycles up to this value were obtained and are shown in figure 9. Clearly the manganese ferrite attains the higher DC magnetization value (11 A m^2 kg^{-1}), followed by magnetite (7.2 A m^2 kg^{-1}) while cobalt ferrite only reaches 2.8 A m^2 kg^{-1}. For the three ferrites the coercive field obtained is below 1 mT.

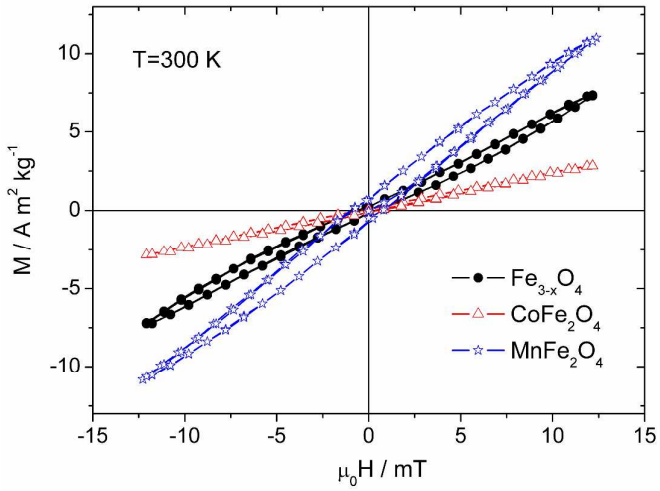

Figure 9. Low fields hysteresis curves for the MFe_2O_4 (M = Co, Fe Mn) samples obtained from the solution. The maximum magnetic field (12.3 mT) was chosen to match the amplitude of AC field used in the hyperthermia measurements.

The $CoFe_2O_4$ nanoparticles obtained after cotton elimination display a higher saturation value as well as higher coercivity at room temperature (see figure 10), when compared with the cobalt ferrite obtained from the solution. The higher magnetization is well explained by the bigger size and lower surface/volume ratio of the particles that approach the bulk behavior. A similar value was reported for nanoparticles with 60 nm diameter after sintering at 1100 ºC. [34] A decrease of the coercivity would be expected for bigger particles, contrary to what is measured experimentally. The increased coercivity is explained by the morphology of these nanoparticles, which have the morphology imposed by the template threads, even after its removal, and present an elongated shape, implying an additional magnetic anisotropy. [39] In the low fields hysteresis cycle (figure 11) the magnetization value at 12.3 mT, 0.9 A m^2 kg^{-1}, is three times smaller than the one of the particles obtained from the solution but is associated with a higher coercivity (1.6 mT). Also, the cycle is not centered in zero magnetization but in -0.1 A m^2 kg^{-1}, indicating that a small fraction of the nanoparticles cannot be rotated up to

12.3 mT, in agreement with the coercive field of 58 mT determined from the hysteresis curve obtained for magnetic fields up to 5.5 T (figure 10).

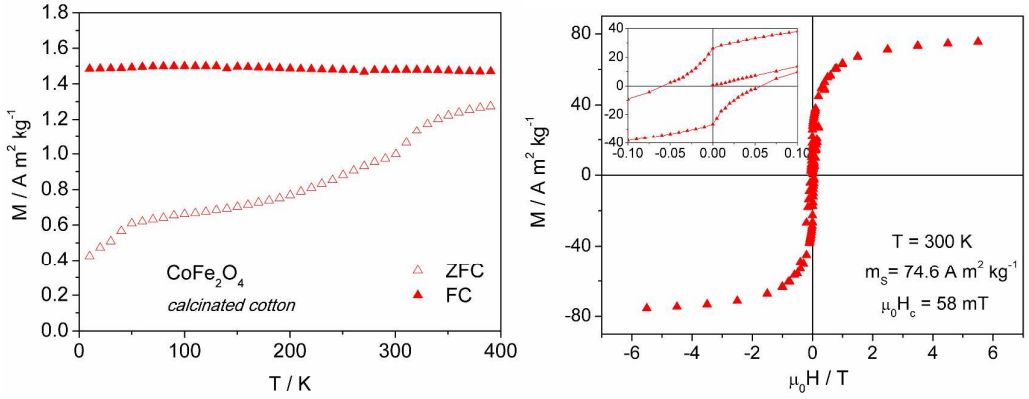

Figure 10. Temperature dependence of the magnetization (left) and hysteresis curve at 300 K for the $CoFe_2O_4$ nanoparticles obtained after cotton elimination.

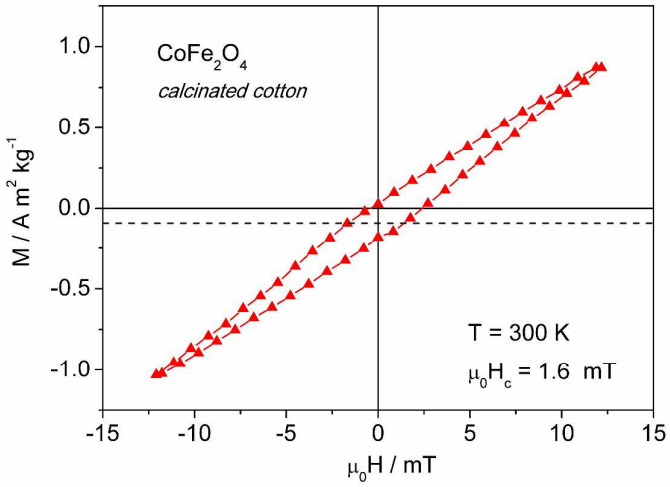

Figure 11. Low field hysteresis curve at 300 K for the $CoFe_2O_4$ nanoparticles obtained from cotton calcination.

The Mössbauer spectra of the MFe_2O_4 (M = Fe, Co, Mn) nanoparticles obtained from the solution are shown in figure 12 and the corresponding Mössbauer parameters are listed in table 3.

Table 3. Mössbauer hyperfine fitting parameters for samples MFe_2O_4 (M = Fe, Co and Mn) obtained from the solution. B_{hf}: magnetic hyperfine field; $<B_{hf}(\sigma)>$: average magnetic hyperfine field (and standard deviation) of the distribution of magnetic splittings; δ: isomer shift; ε: quadrupole shift; ΔE_Q: quadrupole splitting; Γ: line width; I: relative area. Uncertainties in I are less than 2%.

M	**B_{hf}** /T	**$<B_{hf}(\sigma)>$** /T	**δ** /mm s^{-1}	**ε** /mm s^{-1}	**ΔE_Q** /mm s^{-1}	**Γ** /mm s^{-1}	**I** /%
	-	44(9)	0.30(1)	0.08(1)	-	0.31	41
Fe	-	43(7)	0.56(1)	-0.07(1)	-	0.32	35
	47.8(1)	-	0.30(1)	-0.06(1)	-	0.48(2)	24
Co	-	39(11)	0.31(1)	0.00(1)	-	0.40	100
	-	40(11)	0.26(1)	0.01(1)	-	0.30	54
Mn	-	38(11)	0.48(1)	-0.04(2)	-	0.30	40
	-	-	0.33(2)	-	0.69(3)	0.5(1)	6

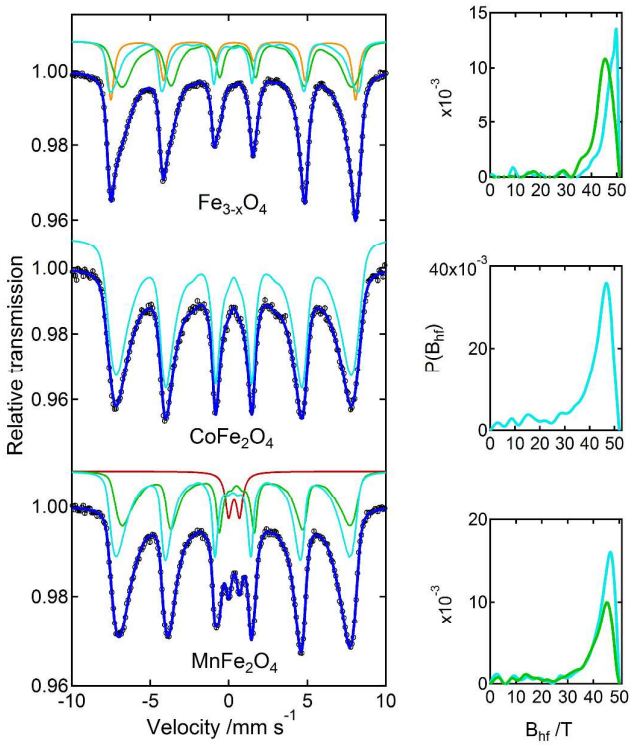

Figure 12. ^{57}Fe Mössbauer spectra collected at 290 K for samples MFe_2O_4 (M = Fe, Co, Mn) obtained from the solution. At the right-hand side of the spectra, the probability distribution of B_{hf} for the iron distributed sites is shown.

All spectra require distributions of the magnetic hyperfine field, B_{hf}, to be properly fitted. In the Fe and Mn compounds, two distributed sextets were adjusted, one with lower isomer shift value (δ) indicating the presence of iron in tetrahedral sites, and the other one with a higher δ value, typical of a mixture of Fe^{2+} and Fe^{3+} in the octahedral sites, although with preponderance of Fe^{3+}. Besides these two sextets, in the $Fe_{3-x}O_4$ spectrum, a third well defined sextet involving around 24% of the iron atoms is also present, with hyperfine parameters close to the ones of maghemite, frequently present in this type of NP. [14,40] In the $MnFe_2O_4$ spectrum, a third well resolved component is necessary, in this case is a

paramagnetic doublet. This paramagnetic component is attributed to the presence of very small NP in the superparamagnetic regime, in agreement with the size distribution obtained from TEM images. The $CoFe_2O_4$ spectrum is well fitted to a single symmetric and distributed sextet (in accordance with the small size of the nanoparticles), and the hyperfine parameters values indicate the presence of Fe^{3+}, both in the tetrahedral and octahedral sites of the spinel structure.

The Mössbauer spectra of the samples obtained after cotton elimination are shown in figure 13 and the corresponding Mössbauer parameters are listed in table 4.

Table 4. Mössbauer hyperfine fitting parameters for the samples obtained from cotton calcination. B_{hf}: magnetic hyperfine field; $<B_{hf}(\sigma)>$: average magnetic hyperfine field (and standard deviation) of the distribution of magnetic splittings; δ: isomer shift; ε: quadrupole shift; Γ: line width; I: relative area. Uncertainties in I are less than 2%.

M	**B_{hf}** /T	**$<B_{hf}(\sigma)>$** /T	**δ** /mm s^{-1}	**ε** /mm s^{-1}	**Γ** /mm s^{-1}	**I** /%
Fe	51.7(1)	-	0.37(1)	-0.21(1)	0.32(1)	100
Co	-	47(7)	0.37(1)	0.02(1)	0.32	62
	48.6(1)	-	0.24(1)	0.01(1)	0.45(1)	38

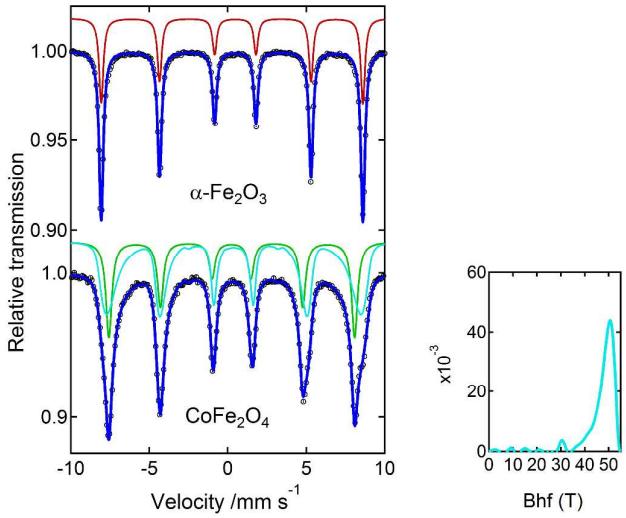

Figure 13. ^{57}Fe Mössbauer spectra collected at 290 K for samples obtained from cotton calcination. At the right-hand side of the spectra, the probability distribution of B_{hf} for the iron distributed site is shown.

The results obtained for the sample M = Fe are in perfect accordance with the hyperfine parameters of hematite, α-Fe_2O_3 [41], corroborating the XRD results. In the case of the M = Co sample, the Mössbauer spectrum is well resolved by two sextets with different isomer shifts, both assigned to Fe^{3+}, in agreement with the results obtained for $CoFe_2O_4$ nanoparticles with sizes around 20 nm. [36] The subspectrum with $\delta = 0.24$ mm s^{-1} is well defined, being attributed to iron in tetrahedral sites; the one with $\delta = 0.37$ mm s^{-1} is distributed and can be assigned to iron in the octahedral sites of the spinel structure. From the relative amounts of each site the formulation $(Fe_{0.76}Co_{0.24})_{tet}(Fe_{1.24}Co_{0.76})_{oct}O_4$ can be deduced, where *tet* and *oct* refer to tetrahedral and octahedral sites, respectively, a distribution close to one previously reported. [28]

3.3 Magnetic hyperthermia performance

The magnetic hyperthermia performance of the different nanoparticles was evaluated by induction heating as described in the experimental details section.

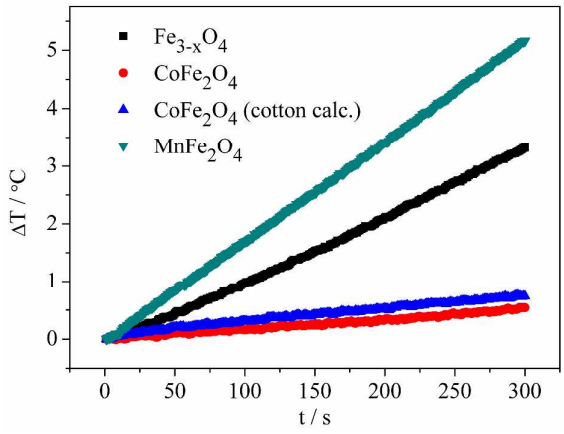

Figure 14. Temperature variation due to magnetic heating over time for MFe_2O_4 (M = Fe, Co, Mn) nanoparticles extracted from the solution and $CoFe_2O_4$ nanoparticles obtained from cotton calcination.

The temperature evolution curves illustrated in figure 14 allowed to evaluate the specific loss power (SLP) for each type of nanoparticles. Several measurements of the temperature evolution with time were obtained for each sample. The results were fitted considering a constant magnetic heating power supplied by the nanoparticles, and assuming linear exchanges between the sample and the environment, whose temperature was assumed to vary linearly between the initial and final recorded temperatures. The fitting expression is

$$T = T_0 e^{-B(t-t_0)} + \left(T_0^{ext} + \frac{h-\alpha}{B}\right)\left(1 - e^{-B(t-t_0)}\right) + \alpha(t - t_0) \qquad (eq.\ 1)$$

where h and B stand, respectively, for the magnetic heating power and linear losses coefficient (both divided by the system heat capacity), T is the sample temperature at instant t, T_0 and T_0^{ext} are the initial sample and environment temperatures at t_0, and alpha is the linear coefficient for the environment temperature variation.

From the fitted parameter h the specific loss power is calculated using the expression:

$$\mathrm{SLP}_{fit} = \mathrm{C_{w+c}}\,\frac{h}{\mathrm{m_{NP}}} \quad (eq.2)$$

where C_{w+c} is the heat capacity of the water and the container and m_{NP} the mass of the magnetic nanoparticles. The values obtained for the different measurements of the same compound were averaged and the final result in each case is listed in table 5. In this table the average SLP obtained from the temperature variation for the first 100 s, a procedure often found in published works, is also presented, along with the magnetic parameters characterizing the low fields hysteresis loop associated with the AC magnetic field amplitude.

Table 5. Specific loss power and magnetization parameters for the MFe_2O_4 (M = Fe, Mn and Co) samples. SLP_{fit}: results taking into account heat exchanges with the environment; SLP_{100s}: values from the temperature variation for the first 100 s; M_{max} and μ_0H_c: maximum value of the magnetization and coercive field of the low fields hysteresis cycle at 300 K; A_{loop}: integral of the minor hysteresis loop; HLP: hysteresis loss power; $<D_{TEM}>$ - average NP sizes extracted from TEM results.

Sample		$<D_{TEM}>$ /nm	SLP_{fit} /W g^{-1}	SLP_{100s} /W g^{-1}	M_{max} /A m^2 kg^{-1}	μ_0H_c /mT	A_{loop} /mJ kg^{-1}	HLP /W g^{-1}
from solution	$Fe_{3-x}O_4$	10	53	54	7.3	0.5	13.5	3.7
	$CoFe_2O_4$	4	10	7	2.8	0.5	4.2	1.2
	$MnFe_2O_4$	5/16	92	88	11	0.9	25	6.9
after cotton elimination	$CoFe_2O_4$	8	14	14	0.9	1.6	3.1	0.78

The results show that the manganese ferrite presents the highest SLP values, 92 W g^{-1}, followed by the magnetite nanoparticles, with a SLP of 53 W g^{-1}. The two cobalt ferrite samples display the lower SLP values.

For the nanoparticles obtained from the solution, the Néel and Brown relaxation times were calculated in water, as reported by Dutz and Hergt [4], using the K_{eff} determined from the maximum in the magnetization curves and assuming a hydrodynamic radius of 1 nm above the NP radius. For a distribution of cobalt ferrite nanoparticles with average diameter of 4 nm, in water, the relaxation contribution is mainly due to the Néel mechanism. The magnetic power associated with the DC hysteresis losses (HLP) was calculated from the minor cycle

area multiplied by the AC field frequency (see table 5). In the case of the cobalt ferrite this contribution is 1.2 W g^{-1} that accounts for 14(2) % of the SLP indicating a significant amount of heat coming from magnetic losses, and supporting the major contribution of magnetization relaxation, since for AC measurements a broadening of the hysteresis curve that increases with frequency is expected. [37] The Brown relaxation must be very small although cannot be completely excluded. Both for the $MnFe_2O_4$ and $Fe_{3-x}O_4$ nanoparticles the calculated DC hysteresis losses are a smaller fraction of the measured SLP (about 7%) indicating a smaller contribution of magnetic losses in these samples as compared to cobalt ferrite and corroborating the lower magnetic anisotropy of these samples.

The manganese ferrite has the lower effective magnetic anisotropy and higher SLP. From the TEM images, the $MnFe_2O_4$ sample can be characterized as having a bimodal size distribution with two average sizes of 16 nm and of 5 nm. Mössbauer data indicates the presence of 6 % of paramagnetic iron nuclei, which was assumed to correspond to the fraction of iron in the smallest $MnFe_2O_4$ NP. Taking into account the volume ratio of the two groups of nanoparticles and the ratio of the Mössbauer Fe relative fractions, the proportion found between the number of NP in each group, N(5 nm)/N(16 nm) ~ 4, agrees with the TEM results (see figure 6). The ZFC curve shape also hints the existence of two types of particles having different behaviours. A fit of this curve allows extracting temperature maxima at 126 K and 400 K that are associated with the magnetic behaviour of the two average sizes NP identified, 5 nm and 16 nm, respectively. Even considering dipolar interactions, the smaller particles are superparamagnetic at 300 K and have a major contribution of Néel losses, while for the larger nanoparticles Brown losses with relaxation times of the order of magnitude of the experimental AC field period, can also contribute to the higher SLP value obtained for this compound. This last conclusion is supported by the measurements carried out in different solvents [42].

The values of specific loss power reported in the literature depend on the synthesis methods and experimental conditions of the hyperthermia measurements, namely the medium and AC field parameters used.

The $Fe_{3-x}O_4$ SLP value is higher or similar to several reported results, taking in account the different experimental conditions of the hyperthermia measurements. Magnetite and maghemite are the most extensively studied NP having different SLP reported values. Using conditions closer to ours, values between 40-90 W g^{-1} (765 kHz and 15 kA m^{-1}) [43] and 46 W g^{-1} (12 kA m^{-1} and 10 kA m^{-1} with 300 kHz and 249 kHz [44]) that are below the results obtained in this work, were reported. Higher values, between 80 and 95 W g^{-1} (10 kA m^{-1} and 249 kHz) [45] were obtained for higher concentrations of Fe_3O_4, namely 4 mg ml^{-1} and 6 mg ml^{-1}.

The comparison of the SLP results obtained for the two $CoFe_2O_4$ nanoparticles shows that the nanoparticles with morphology determined by the cotton template have higher power losses, exceeding in ~50% the value of the smaller ones (obtained from the solution), while the corresponding average NP size changes by a factor of two. Brown relaxation losses scale with the hydrodynamic volume, but the organization of the particles in the form of the cotton threads, promotes interactions between the nanoparticles that will reduce the mobility of the particles limiting this term. On the other hand, the coercive field increases, contrary to what would be expected considering only the volume increase of the magnetic nanoparticles that would imply a decrease of the magnetic anisotropy. Therefore, the higher SLP result of the $CoFe_2O_4$ obtained after cotton elimination is explained by the NP shape modification induced by the cotton role during the synthesis.

In the case of $CoFe_2O_4$, values of 0.07 W g^{-1} at 500 kHz and 5.4 kA m^{-1} were reported for samples with a mean diameter of 8.4 nm [46] and 0.5 W g^{-1} at 111 kHz and 3 kA m^{-1} [47]. The largest reported value, around 400 W g^{-1}, was obtained at a frequency and magnetic field

significantly higher (500 kHz and 37.3 kA m^{-1}) [48] than those used in this work. Thus, although exhibiting the smallest SLP values of the three prepared ferrites, the $CoFe_2O_4$ NP obtained in the present work exhibit good characteristics for magnetic hyperthermia applications.

4. Conclusions

MFe_2O_4 (M = Co, Fe, Mn) nanoparticles were synthesized using a hydrothermal treatment in the presence of medicinal cotton. This methodology gave rise to the production of two sets of nanoparticles for each preparation. Nanoparticles of $Fe_{3-x}O_4$, $CoFe_2O_4$ and $MnFe_2O_4$ with the characteristic spinel structure and mean sizes of 10 nm, 4 nm and 5 nm/16 nm, respectively, were obtained from the solution. Nanoparticles embedded in the cotton were calcinated in air at 550 ºC for cotton elimination, and $CoFe_2O_4$, hematite (α-Fe_2O_3) and a mixture of phases were obtained for the Co, Fe and Mn based samples, respectively.

The Mössbauer results confirmed the production of oxidized magnetite $Fe_{3-x}O_4$ and the presence of iron in both tetrahedral and octahedral sites of the Co and Mn ferrites. For $CoFe_2O_4$ obtained after cotton elimination, the Mössbauer results allowed to deduce the composition $(Fe_{0.76}Co_{0.24})_{tet}(Fe_{1.24}Co_{0.76})_{oct}O_4$.

All the ferrite nanoparticles preserve the ferrimagnetic ordering. The average size and magnetic behaviour indicate that the nanoparticles have single domain magnetic structure.

The ferrite nanoparticles obtained from the solution display good hyperthermia performance, with specific loss power values generally higher than those previously reported for similar nanoparticles measured under comparable conditions. The hyperthermia studies of these samples allow to conclude that the manganese ferrite has the highest specific loss power values, 90 W g^{-1}, although the saturation magnetization value at 300 K is much smaller than the one of the $Fe_{3-x}O_4$ nanoparticles. This result is in agreement with the high initial

susceptibility obtained for the manganese compound, and is also an indication that Néel losses, attributed to the small nanoparticles with superparamagnetic behavior ($<D_{TEM}> \sim 5$ nm), play an important role.

The two compounds obtained from the cotton calcination ($CoFe_2O_4$ and α-Fe_2O_3) exhibit a peculiar morphology resulting from the coalescence and organization of the nanoparticles along threads, highlighting the role of cotton as template. For the threaded cobalt ferrite, the specific loss power values under AC magnetic field are enhanced by 50% when compared to those obtained for the nanoparticles caught from the solution, result that is attributed to the characteristic morphology of the samples.

The use of cotton merged with hydrothermal synthesis turns out to be a simple methodology both to obtain small ferrite nanoparticles (those in solution) and to obtain hematite and $CoFe_2O_4$ with characteristic threadlike morphology, the latter with higher specific loss power. The results obtained in this work show that the methodology used for samples preparation is promising and should be explored through the fine tuning of the experimental conditions to produce nanoparticles with high performance for magnetic hyperthermia applications.

ACKNOWLEDGMENTS

This work was carried out with the support of Portuguese FCT foundation through project PTDC/CTM-BIO/2102/2012 (including grants for S.G. Mendo and A. Alves under the same contract) and by centres grants (BioISI, centre reference: UID/MULTI/04046/2013, and CQB, centre reference: UID/MULTI/00612/2013) from FCT/MCTES/PIDDAC, Portugal.

REFERENCES

1 E. Manova, T. Tsoncheva, Cl. Estournès, D. Paneva, K. Tenchev, I. Mitov and L. Petrov, *Appl. Catal., A,* 2006, **300**, 170-180.

2 V. Polshettiwar, R. Luque, A. Fihri, H. Zhu, M. Bouhrara and J.-M. Basset, *Chem. Rev.*, 2011, **111**, 3036–3075.

3 J. H. Jung, J. H. Lee and S. Shinkai, *Chem. Soc. Rev*., 2011, **40**, 4464–4474.

4 S. Mornet, S. Vasseur, F. Grasset and E. Duguet, *J. Mater. Chem.*, 2004, **14**, 2161-2175.

5 J. Kang, H. Lee, Y.-N. Kim, A. Yeom, H. Jeong, Y. T. Lim and K. S. Hong, *Nanoscale Res. Lett.*, 2013, **8***,* 376.

6 D.-H. Kim, D. E. Nikles, D. T. Johnson and C. S. Brazel, *J. Magn. Magn. Mater.*, 2008, **320***,* 2390-2396.

7 S. Dutz and R. Hergt, *Nanotechnol*., 2014, **25***,* 452001.

8 A. C. Silva, T. R. Oliveira, J. B. Mamani, S. M. F. Malheiros, L. Malavolta, L. F. Pavon, T. T. Sibov, E. Amaro Jr, A. Tannús, E. L. G. Vidoto, M. J. Martins, R. S. Santos and L. F. Gamarra, *Int. J. Nanomed.*, 2011, **6***,* 591-603.

9 A. E. Deatsch and B. A Evans, *J. Magn. Magn. Mater.*, 2014, **354***,* 163-172.

10 G. Baldi, D. Bonacchi, C. Innocenti, G. Lorenzi and C. Sangregorio, *J. Magn. Magn. Mater.*, 2007, **311,** 10-16.

11 A. Jordan, P. Wust, R. Scholz, H. Faehling, J. Krause and R. Felix, Magnetic fluid hyperthermia, in *Scientific and Clinical Applications of Magnetic Carriers,* ed. U. Häfeli, W. Schütt, J. Teller and M. Zborowski, Plenum Press, New York, 1997, pp 569-595.

12 P. Tartaj, M. P. Morales, S. Veintemillas-Verdaguer, T. González-Carreño and C. J. Serna, *J. Phys. D: Appl. Phys.*, 2003, **36**, R182–R197.

13 T. J. Daou, G. Pourroy, S. Bégin-Colin, J.-M. Grenèche, C. Ulhaq-Bouillet, P. Legaré, P. Bernhardt, C. Leuvrey and G. Rogez, *Chem. Mater.*, 2006, **18**, 4399-4404.

14 M. D. Carvalho, F. Henriques, L. P. Ferreira, M. Godinho and M. M. Cruz, *J. Solid State Chem.*, 2013, **201**, 144-152.

15 S. Diodati, L. Pandolfo, A. Caneschi, S. Gialanella and S. Gross, *Nano Res.*, 2014, **7**, 1027-1042.

16 C. Pereira, A. M. Pereira, C. Fernandes, M. Rocha, R. Mendes, M. P. Fernández-García, A. Guedes, P. B. Tavares, J.-M. Grenèche, J. P. Araújo and C. Freire, *Chem. Mater.*, 2012, **24**, 1496-1504.

17 A. Figuerola, R. Di Corato, L. Manna and T. Pellegrino, *Pharmacol. Res.*, 2010, **62**, 126-143.

18 O. Horner, S. Neveu, S. Montredon, J.-M. Siaugue and V. Cabuil, *J. Nanopart. Res.*, 2009, **11**, 1247–1250.

19 S. Xuan, L. Hao, W. Jiang, X. Gong, Y. Hu and Z. Chen, *J. Magn. Magn. Mater.*, 2007, **308,** 210–213.

20 V. Cabuil, V. Dupuis, D. Talbot and S. Neveu, *J. Magn. Magn. Mater.*, 2011, **323,** 1238-1241.

21 S. Komarneni, E. Fregeau, E. Breval and Rustum Roy, *J. Am. Ceram. Soc.*, 1988, **71**, C26-C28.

22 J. Wang, Q. Chen, B. Hou, and Z. Peng, *Eur. J. Inorg. Chem.* 2004, 1165-1168.

23 L. J. Xie, W. Chu, Y. Y. Huang and D. G. Tong, *Mat. Lett.*, 2011, **65**, 153-156.

24 H.-Q. Wang, M.-B. Zheng, J.-H. Chen, G.-B. Ji and J.-M. Cao, *J. Nanotechnol.*, 2010, 479172.

25 D.-Y. Li, Y.-K. Sun, P.-Z. Gao, X.-L. Zhang and H.-L. Ge, *Ceram. Int.*, 2014, **40**, 16529-16534.

26 T. Roisnel and J. Rodriguez-Carvajal, FullProf Suite, 2011.

27 W. Baaziz, B. P. Pichon, S. Fleutot, Y. Liu, C. Lefreve, J.-M. Grenèche, M. Toumi, T. Mhiri and S. Bégin-Colin, *J. Phys. Chem. C*, 2014, **118**, 3795-3810.

28 D. Peddis, N. Yaacoub, M. Ferretti, A. Martinelli, G. Piccaluga, A. Musinu, C, Cannas, G. Navarra, J.-M. Grenèche and D. Fiorani, *J. Phys. Condens. Matter,* 2011, **23**, 426004.

29 B. D. Cullity and C. D. Graham, *Introduction to Magnetic Materials,* ed. John Wiley & Sons, Hoboken, New Jersey, 2nd edn., 2009.

30 R. E. Vandenberghe, R. Vandenberghe, E. De Grave and G. Robbrecht, *J. Magn. Magn. Mater.*, 1980, **15-18**, 1117-1118.

31 P. J. Van der Zaag, A. Noordermeer, M. T. Johnson and P. F. Bongers, *Phys. Rev. Lett.*, 1992, **68**, 3112.

32 U. S. Sharma, R. N. Sharma and R. Shah, *Int. J. Eng. Res. Appl.*, 2014, **4**, 14-17.

33 P. P. Goswami, H. A. Choudhury, S. Chakma and V. S. Moholkar, *Int. J. Chem. Eng.*, 2013, 934234.

34 R. Ianos, *Mat. Lett.*, 2014, **135**, 24-26.

35 M. Houshiar, F. Zebhi, Z. J. Razi, A. Alidoust and Z. Askari, *J. Magn. Magn. Mater.*, 2014, **371**, 43-48.

36 M. Veverka, P. Veverka O. Kaman, A. Lančok, K. Závěta, E. Pollert, K. Knížek, J. Boháček, M. Beneš, P. Kašpar, E. Duguet and S. Vasseur, *Nanotechnol.*, 2007, **18**, 345704.

37 E. Garaio, O. Sandre, J-M Collantes, J. A. Garcia, S. Mornet and F. Plazaola, *Nanotechnol.*, 2015, **26**, 015704.

38 V. Connord, B. Mehdaoui, R. P. Tan, J. Carrey, and M. Respaud, *Rev. Sci. Instrum.*, 2014, **85**, 093904.

39 J. L. Dormann, D. Fiorani and E. Tronc, Magnetic relaxation in fine-particle systems, in *Advances in Chemical Physics,* ed. I. Prigogine and S. A. Rice, John Wiley & Sons, Hoboken, New Jersey, 1997, vol. 98.

40 J. S. Salazar, L. Perez, O. Abril, L. T. Phuoc, D. Ihiawakrim, M. Vazquez, J.-M. Grenèche, S. Bégin-Colin and G. Pourroy, *Chem. Mater.*, 2011, **23**, 1379-1386.

41 S. J. Oh, D. C. Cook and H. E. Townsend, *Hyperfine Interact.*, 1998, **112**, 59-65.

42 L. P. Ferreira, A. F. Alves, M. M. Cruz, S. G. Mendo, R. Gigante, S. Biscaia, T. Viana, M. Franco, M. Godinho, G.R. Mitchell, M.D. Carvalho, to be published.

43 M. Filippousi, M. Angelakeris, M. Katsikini, E. Paloura, E. I. Efthimiopoulos, Y. Wang, Y. D. Zamboulis and G. V. Tendeloo, *J. Phys. Chem. C*, 2014, **118**, 16209-16217.

44 Y. V. Kolen'ko, M. Bañobre-López, C. Rodríguez-Abreu, E. Carbó-Argibay, A. Sailsman, Y. Piñero-Redondo, M. F. Cerqueira, D. Y. Petrovykh, K. Kovnir, O. I. Lebedev and J. Rivas, *J. Phys. Chem. C*, 2014, **118**, 8691-8701.

45 M. A. Vergés, R. Costo, A. G. Roca, J. F. Marco, G. F. Goya, C. J. Serna and M. P. Morales, *J. Phys. D: Appl. Phys.*, 2008, **41**, 134003.

46 M. Jeun, S. Bae, A. Tomitaka, Y. Takemura, K. H. Park, S. H. Paek and K.-W. Chung, *Appl. Phys. Lett*., 2009, **95**, 082501.

47 I. Andreu, E. Natividad, C. Ravagli, M. Castro and G. Baldi, *RSC Adv.*, 2014, **4**, 28968–28977.

48 J.-H. Lee, J.-T. Jang, J.-S. Choi, S. H. Moon, S.-H. Noh, J.-W. Kim, J.-G. Kim, I.-S. Kim, K. I. Park and J. Cheon, *Nat. Nanotechnol.,* 2011, **6**, 418–422.